ROYAL SOCIETY
OF CHEMISTRY

Check for updates

# Tungsten nitride on a porous carbon support as a highly durable electrocatalyst for the hydrogen evolution reaction

Shankar Baskaran, Gokul Pandiyan Mageswari, J. Anjana [ID] and
Azhagumuthu Muthukrishnan [ID] *

The hydrogen evolution reaction is a key reaction in the field of sustainable energy, and platinum is recognised as a state-of-the-art catalyst for this reaction. The cost and scarcity of platinum drive us to look for low-cost and effective alternatives. Among the various metal nitrides, tungsten nitride has been less explored as an HER electrocatalyst despite its stability under extreme pH conditions. WN–carbon composites were synthesised using urea as a nitrogen precursor, and the synthesised WN/NC catalyst exhibits a lower HER overpotential of 200 mV in an acidic medium and 230 mV in an alkaline medium. The mass activity was estimated as 24.2 A $g^{-1}$ in 0.5 M $H_2SO_4$, which is much higher than the mass activity in 1 M KOH electrolyte (13.5 A $g^{-1}$). A homemade water electrolysis system demonstrates that the WN–carbon composite-coated carbon electrode exhibits hydrogen evolution up to 770 mL $min^{-1}$ $g_{cat}^{-1}$ at a constant current density of 100 mA $cm^{-2}$. The results demonstrate that the WN with an appropriate carbon support may be a promising alternative to platinum-based electrocatalysts for the hydrogen evolution reaction.

## Introduction

With growing concerns over global warming and environmental degradation, a shift towards renewable and sustainable energy sources has become mandatory.[1] Hydrogen is identified as a clean source of energy due to its environmental friendliness, earth abundance and high energy density.[2,3] Despite various methods currently employed to produce hydrogen, fossil fuels are the primary source of hydrogen production.[4] Water electrolysis is one of the desirable methods for hydrogen production as it avoids greenhouse gas emissions. However, the sustainability of the green hydrogen production depends on the energy source (solar, wind, hydro, biomass, *etc.*).

Water electrolysis is an energy-intensive process that needs appropriate catalysts to minimise the energy intake and to split the water into $H_2$ and $O_2$. Water electrolysis involves hydrogen and oxygen evolution reactions (HER and OER) at the cathode and anode of the water electrolyser, respectively.[5] The source of hydrogen is usually $H^+$ in an acidic medium and $H_2O$ in a neutral/alkaline medium. Generally, the HER proceeds *via* two pathways: (i) the adsorption of $H^+/H_2O$ on the active site (Volmer step), followed by the recombination of two nearby adsorbed hydrogens to evolve $H_2$ (Tafel step) or (ii) the

adsorption of $H^+/H_2O$ on the active site (Volmer step), followed by combining with another $H^+/H_2O$ near the surface to evolve $H_2$ (Heyrovsky step).[6] The former mechanism involves two active sites, whereas the latter needs only one active site. The platinum-based materials are the state-of-the-art catalysts for the HER.[7] Transition metal-based materials (TMX, where X = O, S, Se, Te, N, P, C and B) are predominantly explored for HER electrocatalysis due to their metallic-like conductivity and corrosion resistance under extreme pH conditions, as well as their low cost and availability.[8–10] The design principles for enhancing the HER activity of TMX catalysts are well-documented in the literature.[11] 2D transition metal chalcogenides are widely recognised for their HER activity and stability.[12] Alloying or combining with precious metals substantially improves the HER activity.[13,14]

Among the above-mentioned non-precious metal catalysts, transition metal nitrides (TMN) are more attractive due to their unique physical and chemical characteristics, which increase the inherent activity of the catalyst.[15–17] A theoretical analysis of the HER activity on various metal nitrides demonstrates that TaN showed the lowest overpotential towards the HER.[18] The experimental results of HER activity on various mono and bimetallic nitrides are summarised in review articles.[19–22] The monometallic nitrides, such as $Ni_3N_{1−x}$,[23] $Mo_5N_6$,[24] TaN,[25] TiN,[26] *etc.*, show the best HER activity. Besides, the bimetallic nitrides were reported for their enhanced HER activities in $Co_xNi_yN$,[27] $FeNi_3N$,[28] $Ni_2MO_3N$[29] and $NiTiN_x$.[30]

*School of Chemistry, Indian Institute of Science Education and Research,*
*Maruthamala P.O., Vithura-695551, Thiruvananthapuram, Kerala, India.*
*E-mail: muthukrishnan@iisertvm.ac.in*

Among various metal nitrides, tungsten nitrides draw attention for their flexible phase/electronic structure, noble metal-like catalytic behaviour and earth abundance.[31] Also, tungsten nitride-based materials exhibit excellent stability under both acidic and alkaline conditions.[32] Wang and co-workers have synthesised WN nanoarrays on carbon cloth via $N_2$ plasma treatment, which requires a small overpotential ($\eta_{10}$ = 130 mV) with exceptional stability.[33] Similarly, $W_2N$/WP carbon nanofibers exhibit better activity and stability in both alkaline and acidic electrolytes with an $\eta_{10}$ value of 157 mV.[34] A MOF-derived Co/WN[35] and WN/rGO on an N,P-doped carbon composite[36] exhibit a minimum overpotential of 76 and 85 mV, respectively.

Herein, the importance of WN with a carbon support is discussed. A simple one-step pyrolysis process was adopted to synthesise the hexagonal phase of WN using $Na_2WO_4$, urea and conductive carbon. The uniformly distributed WN nanoparticles were synthesised on the carbon support. The tungsten nitride carbon (WN/NC) composites were analysed for their HER activity in both acidic and alkaline media.

## Methodology

The WN/NC composites were synthesised by a high-temperature pyrolysis method. The Ketjen Black 300J (KB) conductive carbon (100 mg) was dispersed in 20 mL of deionised water under constant stirring, and 20 mL aqueous solution of 0.05 M $Na_2WO_4 \cdot 2H_2O$ (Avra Chemicals) was added to it. Furthermore, the mixture was heated to 100 °C under continuous stirring to evaporate the water, allowing effective dispersion of tungsten precursor on the carbon matrix. The composite material was mixed with urea (a composite-to-urea ratio of 1:10) and heated to 900 °C for 2 hours under a $N_2$ atmosphere. Then, the pyrolysed material was washed with deionised water, designated as WN/NC-1. A few other materials were synthesised by changing the initial carbon content to 300 and 500 mg, referred to as WN/NC-2 and WN/NC-3, respectively. Apart from this, a control sample was synthesised by mixing $Na_2WO_4 \cdot 2H_2O$, KB and urea (3:1:40), and the same procedure was followed as mentioned above to yield WN/NC-1A. The formation of WN from the precursor is probed using powder XRD. The temperature-dependent XRD pattern indicates that WN forms at 900 °C (Fig. S1). The TGA curves demonstrate that the urea decomposed to ammonia, which combines with $WO_3$ (formed from the decomposition of $Na_2WO_4 \cdot 2H_2O$) to form $\beta$-$W_2N$. Later, $\beta$-$W_2N$ transformed into $\delta$-WN at higher temperatures.

The synthesised WN/NC composites were analysed using a X-ray diffraction (XRD) technique (PANalytical Empyrean XRD with a Cu K$\alpha$ source, $\lambda$ = 1.5406 Å) to understand the structure of the materials. Raman spectroscopy was performed using an HR800 LabRAM confocal Raman spectrometer. The morphology of the samples was studied using scanning electron microscopy (SEM, Nova-NANOSEM 450) and transmission electron microscopy (TEM, FEI Tecnai G2 Spirit Bio-Twin TEM 300 kV). Thermogravimetric analysis (TGA) was performed using a Hitachi thermal analysis system, STA200. The surface area and porosity analyses were performed using the Micromeritics 3Flex system at 77 K using liquid nitrogen. The X-ray photoelectron spectroscopy (XPS) measurements were performed using a PHI VersaProbe 4 instrument with an Al-K$\alpha$ excitation source in a CAE mode with a pass energy of 50 eV.

The electrochemical evaluation of the HER was performed in both acidic and alkaline media using a potentiostat (Origalys OGF500) and an electrode rotator (PINE Instruments). A 5 mg sample was measured and transferred into a vial containing 150 μL of isopropanol, 150 μL of Milli-Q water and 50 μL of 5 wt% Nafion (D521) solution. This mixture was sonicated under ice-cold conditions for 30 minutes to ensure thorough dispersion and the formation of a homogeneous ink. As reported previously,[37] 6.9 μL of uniformly dispersed catalytic ink was coated on the glassy carbon rotating ring electrode (RDE, 5.6 mm diameter). The estimated loading density of the catalyst was 0.4 mg cm$^{-2}$. Finally, the electrode was dried under a $N_2$ atmosphere. This catalyst-modified glassy carbon disk, Ag/AgCl (sat. KCl), and carbon cloth wrapped around a graphite rod served as the working, reference and counter electrodes, respectively. Furthermore, the potentials were corrected to a reversible hydrogen electrode (RHE) using the pH of the electrolyte. The linear sweep voltammogram (LSV) experiment was performed by scanning the potential from 0 V to −0.6 V in both alkaline (1 M KOH) and acidic (0.5 M $H_2SO_4$) electrolytes under deaerated conditions at a scan rate of 5 mV s$^{-1}$. A cyclic voltammogram experiment was performed in the same region as the electrochemical pre-treatment.

A homemade water electrolyser was assembled using catalyst-coated carbon paper (Toray) as the cathode in both acidic and alkaline electrolytes with a loading density of 1 mg cm$^{-2}$. The area of the electrode was calculated to be 3 cm$^2$. The Ni-foam was used in alkaline electrolyte due to the intrinsic activity of the Ni electrodes towards the OER, and $IrO_2$-coated Pt-mesh was used as the anode in acidic electrolyte due to its stability. Both anodic and cathodic compartments were separated using an alkaline exchange membrane (alkaline medium) and Nafion-212 membrane (acidic medium). A chronopotentiometry experiment was performed at 10 mA cm$^{-2}$ (for 100 h) and 100 mA cm$^{-2}$ (for 24 h) to evaluate the stability of the catalyst in real-time application.

## Results and discussion

The materials were fully characterised using spectroscopic and microscopic techniques. First, the compounds were characterised using powder XRD, as shown in Fig. 1(a). The XRD pattern exhibits distinct diffraction peaks at $2\theta$ values of 31.7° (001), 35.8° (100), 48.5° (101), and 64.3° (110), indicating the hexagonal phase of WN ($\delta$-WN phase).[35] This shows the phase purity and crystalline nature of the WN/NC composites. The pristine WN without a carbon support was synthesised, and its XRD pattern exhibits a face-centred cubic $W_2N$ structure ($\beta$-$W_2N$), as shown in Fig. 1(a). Hence, the carbon support facilitates the formation of the $\delta$-WN phase. The materials were
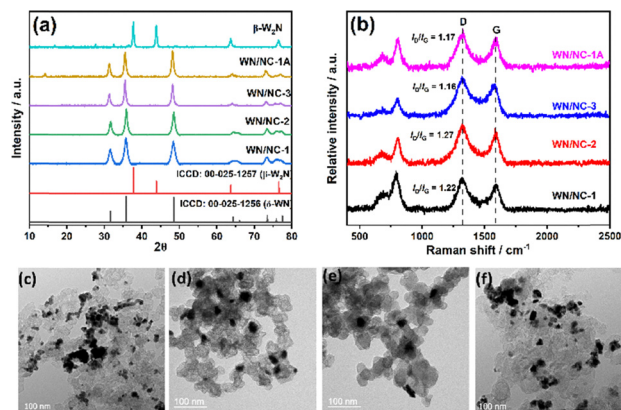
Fig. 1  (a) Powder XRD patterns of the WN/NC catalysts and (b) their Raman spectra. The TEM images of the (c) WN/NC-1, (d) WN/NC-2, (e) WN/NC-3 and (f) WN/NC-1A catalysts.
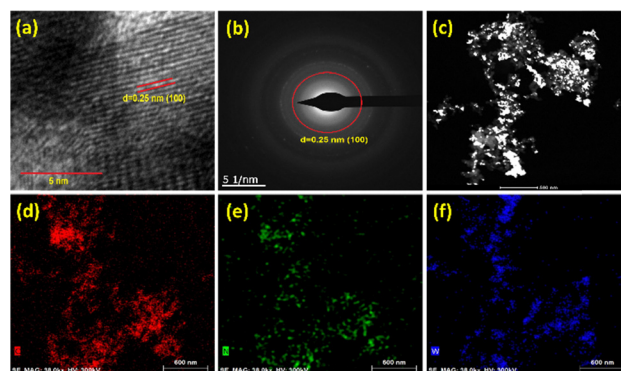


Fig. 2  High resolution transmission electron microscopy analysis of the WN/NC-1 catalyst: (a) lattice fringes, (b) selected area electron diffraction (SAED) pattern, (c) high-angle annular dark-field scanning transmission electron microscopy (HAADF-STEM) image and (d)–(f) elemental mapping of carbon (red), nitrogen (green) and tungsten (blue) elements.

further analysed using Raman spectra, as shown in Fig. 1(b). Typically, the defect density of the carbon support was evaluated using the intensity ratios of the D and G bands ($I_D/I_G$). The $I_D/I_G$ values of all the materials vary from 1.16 to 1.27, indicating a slight decrease from the pristine carbon support (KB) value.[38] Besides, two additional peaks at 680 cm$^{-1}$ and 800 cm$^{-1}$ were observed, corresponding to WN.[39] Though tungsten nitride was not Raman active, these two peaks arise due to the presence of anion vacancies in the WN structure.[40] The intensity is decreased as the tungsten loading decreases.

The SEM images reveal a rough surface morphology of the materials, which may be due to the agglomeration of the smaller particles (Fig. S2). The high-resolution TEM images exhibit a uniform dispersion of WN particles on the carbon support (Fig. 1(c)–(f)). There is no significant difference observed between the composites WN/NC-1 (W/KB as the precursor) and WN/NC-1A (Na$_2$WO$_4$·2H$_2$O + KB + melamine mixture as the precursor), as both composites have almost similar tungsten content. This clearly demonstrates that the method of synthesis does not affect the material's morphology. Conversely, the carbon support plays a crucial role in morphology, as β-W$_2$N synthesised without carbon leads to a large aggregation that tends to form a sheet-like morphology (Fig. S3). The lattice fringes of WN/NC-1 exhibit an interplanar distance of 0.25 nm, which corresponds to the 100 plane of WN, and the selected area electron diffraction (SAED) pattern also exhibits a similar $d$-spacing value of 0.25 nm (Fig. 2(a) and (b)).[41] This strongly suggests the formation of tungsten nitride in the composite material. The high-angle annular dark-field scanning transmission electron microscopy (HAADF-STEM) image reveals a highly interconnected morphology, with brighter spots indicating the presence of tungsten in the carbon composite (Fig. 2(c)). The presence of tungsten and nitrogen in the carbon matrix was further confirmed with elemental mapping using electron energy loss spectroscopy (EELS). This indicates the homogeneous dispersion of W, N and C in the composite material, where tungsten is present in both nitrogen and carbon concentrated areas, as in Fig. 2(d)–(f).

The N$_2$-sorption isotherm was used to estimate the surface area and porosity of the materials. The isotherms are analysed using the Brunauer–Emmett–Teller (BET) method at 77 K. The adsorption isotherms indicate that the materials exhibit a type-IV adsorption isotherm with H4 hysteresis loop, suggesting the presence of mesopores in the material (Fig. 3(a)).[42] It is also observed that the surface area increases with the carbon content. The WN/NC-1 catalyst exhibits a surface area of 128.4 m$^2$ g$^{-1}$, whereas the WN/NC-3 catalyst has the highest surface area of 480.2 m$^2$ g$^{-1}$ (Table S1). The non-local density functional theory (NLDFT) pore size analysis revealed that WN/NC-1 and WN/NC-1A did not exhibit any clear micropores due to their lower carbon content. However, WN/NC-2 and WN/NC-3 exhibit clear microporosity, as indicated by the pore size distribution plot in Fig. 3(b). Although the mesopore distribution shows pore sizes from 3 to 11 nm, the maximum pores have a diameter of 3 nm. The NLDFT method indicates the presence of mesopores in samples with a lower carbon content, whereas the microporosity increases with the carbon content.

The absolute weight percentage of tungsten present in the composite was quantified using a thermogravimetric analysis experiment performed in an air atmosphere (Fig. 3(c)). A slight increase in the weight percentage was observed between 400 °C and 500 °C, corresponding to the conversion of WN to WO$_3$. Later, a significant weight loss was observed after 500 °C due to the removal of carbon as CO$_2$. The residual weight percentage corresponds to WO$_3$, as confirmed by powder XRD (Fig. S4). The weight percentages of WN are calculated from the WO$_3$ obtained from TGA, and the values are 59.1% (WN/NC-1), 37.2% (WN/NC-2), 31.5% (WN/NC-3), and 64.5% (WN/NC-1A).

The X-ray photoelectron spectroscopic technique is used to analyse the chemical environment and oxidation states of the elements. The survey spectrum of WN/NC-1 indicates the presence of C, N, O, and W elements, with relative percentages of 90.3%, 3.3%, 4.6%, and 1.8%, respectively (Fig. S5). The core-level C-1s spectrum confirms the presence of typical sp$^2$-C and sp$^3$-C at 284 and 284.9 eV, respectively (Fig. 3(d)). The N-1s XPS shows the presence of W–N with a peak at 396.9 eV coexisting
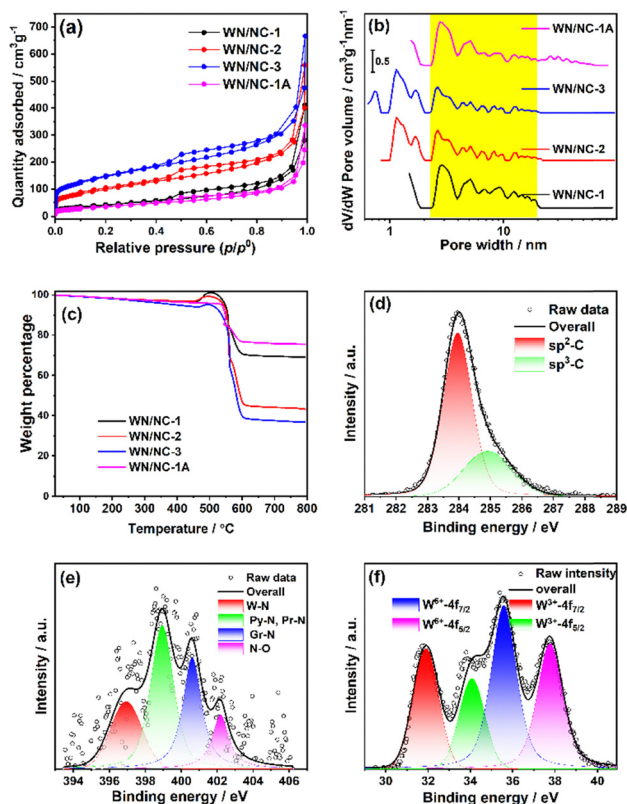
Fig. 3 (a) The N$_2$-sorption isotherms of the WN/NC catalysts and (b) their NLDFT pore size distribution plot. (c) Thermogravimetric plots of the WN/NC catalysts in an air atmosphere. The (d) C-1s, (e) N-1s and (f) W-4f XPS of WN/NC-1 and their deconvoluted peaks.

with pyridinic nitrogen atoms (Py–N, 399.0 eV), graphitic nitrogen atoms (Gr–N, 400.7 eV) and nitrogen oxides (402.2 eV) (Fig. 3(e)). The relatively lower percentage of W–N peak can be rationalised due to the formation of tungsten oxide on the surface. The tungsten XPS peaks were characterised using the W-4f peak.[43] The peak at 31.9 eV corresponds to the W-4f$_{7/2}$ peak in the WN. The W-4f$_{5/2}$ peak appears at 34.1 eV ($\Delta$ = 2.2 eV). The peaks appearing at 35.6 and 37.8 eV ($\Delta$ = 2.2 eV) correspond to the W-4f$_{7/2}$ and W-4f$_{5/2}$ of tungsten oxide, which forms as a passivating layer on the surface (Fig. 3(f)).

The hydrodynamic voltammetry technique was employed to analyse the HER activity of the WN/NC catalysts in a 0.5 M H$_2$SO$_4$ electrolyte, as shown in Fig. 4(a). The WN/NC-1 catalyst exhibits a lower overpotential of 200 mV to achieve a current density of 10 mA cm$^{-2}$, whereas the WN/NC-2 and WN/NC-3 catalysts exhibit a slightly higher overpotential of 220 mV and 225 mV, respectively. This reveals that the loading of tungsten plays a crucial role in enhancing HER activity, as WN/NC-2 and WN/NC-3 have a relatively lower tungsten content than the WN/NC-1 catalyst. A few control experiments were carried out to understand the active sites and the synergy between the carbon support and the WN. The pristine W$_2$N (Fig. 1(a) and Fig. S3) and N-doped carbon (Fig. S6) were synthesised and characterised using XRD and SEM. Both materials exhibit poor HER activity with an overpotential greater than 600 mV (Fig. S7).
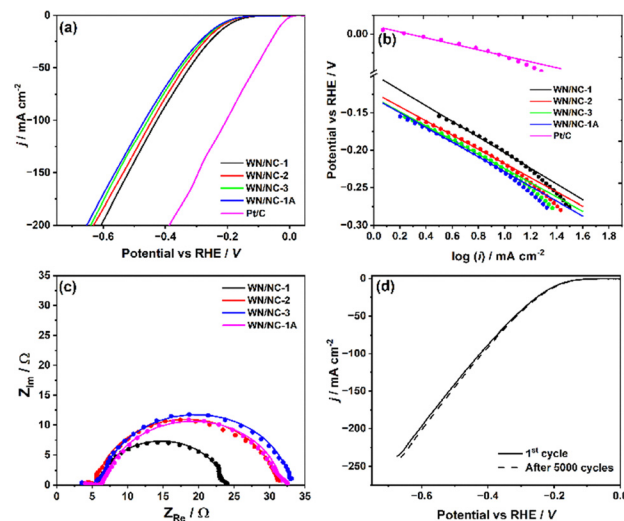


Fig. 4 Linear sweep voltammogram of the WN/NC catalysts in N$_2$-saturated 0.5 M H$_2$SO$_4$ electrolyte at a scan rate of 5 mV s$^{-1}$ and 1600 rotational speed, and the (b) Tafel plots, (c) electrochemical impedance spectroscopy analysis of the WN/NC catalysts at an overpotential of 190 mV and (d) linear sweep voltammogram of the HER on the WN/NC-1 catalyst before and after 5000 cycles of accelerated durability test (ADT).

Hence, the synergy between the carbon support and WN plays a crucial role in enhancing the activity by increasing the conductivity and surface area of the catalysts. On the other hand, the WN/NC-1A catalyst exhibits 30 mV higher overpotential than the WN/NC-1 catalyst. Despite having a similar tungsten content and morphology, the difference in the HER activity indicates the importance of the synthetic method. The benchmark Pt/C catalyst was coated on the RDE electrode with a loading density of 15 μg$_{Pt}$ cm$^{-2}$, which exhibits an onset potential of −0.03 V.

The HER activity of the catalysts is evaluated using the area-specific and mass-specific kinetic current densities ($j_k$). The electrochemical surface area (ECSA) was estimated from the double-layer capacitance as reported earlier (Fig. S8),[44] and the values are reported in Table 1. The ECSA of the benchmark Pt/C catalyst was estimated from the hydrogen under potential deposition (H-UPD) region (Fig. S9). Linear sweep voltammetry was performed at different rotational speeds, and a subtle or no change was observed at lower current densities (Fig. S10).

Table 1 The area- and mass-specific kinetic current densities of the HER on different WN/NC catalysts in 0.5 M H$_2$SO$_4$ electrolyte at the onset potential (−0.2 V) and their Tafel slope values

| Materials | ECSA (cm$^{-2}$) | $j_k$ (μA cm$^{-2}$) | $j_k$ (A g$^{-1}$) | Tafel slope (mV dec$^{-1}$) |
|---|---|---|---|---|
| WN/NC-1 | 29.4 | 80.8 | 24.2 | −105 |
| WN/NC-2 | 39.4 | 42.1 | 16.9 | −95 |
| WN/NC-3 | 50.9 | 27.9 | 14.2 | −95 |
| WN/NC-1A | 24.2 | 53.9 | 13.3 | −99 |
| Pt/C[a] | 0.89 | 1817.1 | 218.0 | −40 |

[a] The ECSA is calculated from the H-UPD region, and the $j_k$ values are calculated at −0.02 V.

Therefore, the reaction is under kinetic control, and the current is considered as kinetic current. The area-specific kinetic current densities were calculated for all the materials (at −0.2 V) from the linear sweep voltammograms. Among all the materials, the highest ECSA-specific and mass-specific $j_k$ values were obtained for WN/NC-1, as 80.8 μA cm$^{-2}_{\text{ECSA}}$ and 24.2 A g$^{-1}$, respectively. These values are significantly higher than those of the other WN/NC materials. While increasing the carbon content decreases the area- and mass-specific activity, this highlights the importance of tungsten loading. The turn-off frequency (TOF)[45] was calculated for the WN/NC-1 catalysts at an overpotential of 0.2 V, based on the tungsten content estimated from TGA and XPS. It was estimated as 0.175 s$^{-1}$ (for a 54.3 μg loading of the entire tungsten content, estimated from TGA) and 5.42 s$^{-1}$ (for a 1.75 μg loading of the surface tungsten content, estimated from XPS). The benchmark Pt/C catalyst shows the highest $j_k$ value near the onset region (−0.02 V), as shown in Table 1.

The kinetic analysis of the HER on the WN/NC catalysts was performed using the Tafel plot (Fig. 4(b)). Since the Tafel slope values of all the composites were in the range of −95 to −105 mV dec$^{-1}$, the HER follows the Volmer–Heyrovsky route *via* the adsorption of hydrogen with 1e$^-$ reduction. A subsequent proton/electron transfer *via* the Heyrovsky step leads to the evolution of molecular H$_2$, wherein the Volmer step is the rate-determining step.[46,47] On the contrary, the Pt/C catalyst follows the Volmer–Tafel mechanism, wherein the two nearby adsorbed hydrogens form an H$_2$ molecule. The kinetic feasibility was analysed using electrochemical impedance spectroscopy (EIS). The faradaic charge transfer resistance is obtained from a semicircle of the complex plane plot at an overpotential of 0.19 V (Fig. 4(c)). A semicircle was fitted with an Armstrong–Henderson equivalent circuit modified with a constant phase element (CPE) to account for non-ideality of the surface (Fig. S11).[48–50] This equivalent circuit consists of two resistance parameters apart from the solution resistance. This is due to the contribution of pseudocapacitive adsorption of H atoms at a specified potential during the course of reaction, which tends to pseudo-resistance ($R_{ps}$).[51] The WN/NC-1 catalyst exhibits a lower charge transfer resistance ($R_{ct}$) of 18 Ω, whereas WN/NC-2, WN/NC-3 and WN/NC-1A show 25.5 Ω, 26.5 Ω and 25.1 Ω, respectively. The lower $R_{ct}$ suggests facile electron transfer. The $R_{ps}$ is found to be <1 Ω, which is highly insignificant in comparison with $R_{ct}$, resulting in a single semicircle in the complex plane plot. The values of the resistive components ($R_s$, $R_{ct}$ and $R_{ps}$) are given in Table S2. The long-term durability of the WN/NC-1 catalyst was analysed using an accelerated durability test (ADT) by a cyclic voltammetry experiment in the HER on and off regions (−0.1 V to −0.4 V) for 5000 cycles at a scan rate of 50 mV s$^{-1}$. The WN/NC-1 and WN/NC-1A catalysts exhibited no degradation in their activity, confirming their excellent stability (Fig. 4(d) and Fig. S12).

The HER performance of the WN/NC catalysts was also analysed in an alkaline medium. The hydrodynamic linear sweep voltammograms of the WN/NC catalysts in an alkaline medium are shown in Fig. 5(a). Similar to the acidic medium,
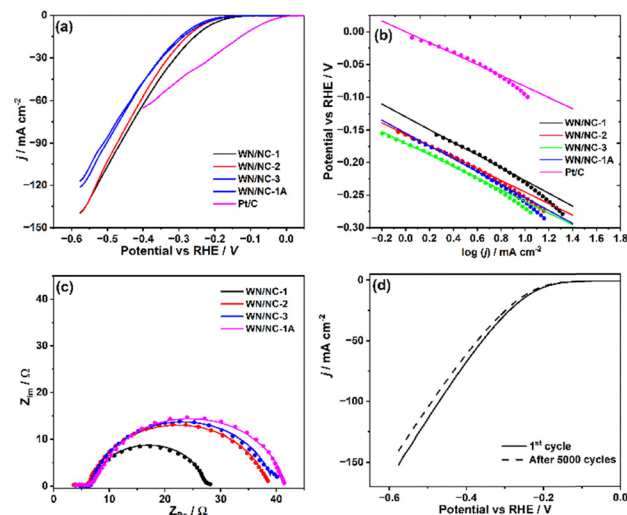


Fig. 5 (a) Linear sweep voltammogram of the WN/NC catalysts in N$_2$-saturated 1 M KOH as the electrolyte, (b) its Tafel plots, (c) electrochemical impedance spectroscopy analysis of the WN/NC catalysts at an overpotential of 200 mV and (d) linear sweep voltammogram of the WN/NC-1 catalyst before and after 5000 cycles of accelerated durability test (ADT).

the WN/NC-1 catalyst exhibits a lower overpotential of 230 mV to reach a current density of 10 mA cm$^{-2}$. As the tungsten content decreases, a significant decrease in the catalyst's performance is observed. The control samples (WN without carbon support and N-doped carbon) show a similar trend to that of the acidic medium (Fig. S13). The ECSAs of the catalysts are given in Table 2 (Fig. S14 and S15). The $j_k$ values are calculated from the hydrodynamic voltammetry, considering that the reaction at the onset region is kinetically controlled (Fig. S16). The ECSA-specific and mass-specific $j_k$ values are calculated as described in the acidic electrolyte at −0.2 V (Table 2). These values indicate that the HER is more active in the acidic medium than in the alkaline electrolyte. Similar to the acidic electrolyte, the TOF values are calculated for the WN/NC-1 catalyst at an overpotential of 0.2 V. The TOF is estimated to be 0.094 s$^{-1}$ (from TGA) and 2.90 s$^{-1}$ (from XPS). Similar tungsten-based materials reported in the literature are given in Table 3. The overpotentials at 10 mA cm$^{-2}$ of similar materials reported in the literature are compared. Although a few materials show a smaller overpotential compared to this

Table 2 The area- and mass-specific kinetic current densities of the HER on different WN/NC catalysts in 1 M KOH electrolyte at the onset potential (−0.2 V) and their Tafel slope value

| Materials | ECSA (cm$^{-2}$) | $j_k$ (μA cm$^{-2}$) | $j_k$ (A g$^{-1}$) | Tafel slope (mA dec$^{-1}$) |
|---|---|---|---|---|
| WN/NC-1 | 34.0 | 38.9 | 13.5 | −98 |
| WN/NC-2 | 54.8 | 14.2 | 7.9 | −89 |
| WN/NC-3 | 78.5 | 7.0 | 5.6 | −90 |
| WN/NC-1A | 19.9 | 37.3 | 7.6 | −99 |
| Pt/C[a] | 0.76 | 548.3 | 56.3 | −84 |

[a] The ECSA is calculated from the H-UPD region, and the $j_k$ values are calculated at −0.02 V.

**Table 3** Tungsten-based HER catalysts reported in the literature

| S. no. | Materials | $\eta_{10}$ (0.5 M $H_2SO_4$)/mV | $\eta_{10}$ (mV) (1 M KOH)/mV | Ref. |
|---|---|---|---|---|
| 1 | WN nanowires | 134 | 130 | 33 |
| 2 | Co/WN | — | 76 | 35 |
| 3 | $W_2C$/WP@NC-2 | 196 | 116 | 52 |
| 3 | CoW/NC | — | 240 | 53 |
| 4 | P-WN/rGO | 85 | — | 36 |
| 5 | Co3W-WN/rGO | 172 | 170 | 54 |
| 6 | P-Ni/WN | — | 45 | 55 |
| 7 | W2N/WC | 130 | 164 | 56 |
| 8 | Co-NC@W2N | — | 55 | 57 |
| 9 | WC@C/NF | 208 | 124 | 58 |
| 10 | WN/NC-1 | 200 | 230 | This work |

study, those potential values are iR-corrected, and the loading density is typically much higher (for example, 1 mg cm$^{-2}$).

The Tafel slopes for the WN/NC materials vary from −90 to −100 mV dec$^{-1}$ (Fig. 5(b)), which are more or less similar to the Tafel slope values estimated in acidic medium. Hence, it follows the Volmer–Heyrovsky mechanism. The Tafel slope of the Pt/C catalysts was estimated to be −84 mV dec$^{-1}$. Unlike in an acidic medium, the Pt/C catalyst follows the Volmer–Heyrovsky mechanism. The EIS shows a similar trend to that of the complex plane plot in acidic medium (Fig. 5(c) and Table S3). The long-term durability of the WN/NC-1 catalyst was also analysed in alkaline electrolyte using ADT with a similar protocol as mentioned above. WN/NC-1 exhibits an excellent stability over 5000 cycles with only a 10 mV negative shift from its overpotential (Fig. 5(d)). Conversely, the WN/NC-1A catalyst shows a 60 mV shift after 5000 cycles, illustrating the need for impregnating WN on the carbon support at the precursor stage (Fig. S17).

Since the WN/NC-1 catalyst exhibits lower overpotential and higher stability towards the HER in acidic and alkaline electrolytes, it is used as a cathode material in both PEM and AEM water electrolysers. The PEM water electrolyser was assembled with WN/NC-1 catalyst-coated carbon paper as the cathode and $IrO_x$-coated Pt mesh as the anode electrodes; both the anode and cathode compartments were separated by a Nafion-212 membrane. The typical electrolyser setup is illustrated in the SI (Fig. S18). The electrocatalytic hydrogen production was performed by a chronopotentiometry experiment at a constant current density of 10 mA cm$^{-2}$. It exhibits a cell potential of −1.78 V with

exceptional stability for more than 100 hours (Fig. 6(a)). Hydrogen gas liberated from the cathode compartment was estimated using the eudiometry method. The inset of Fig. 6(a) shows the plot of the volume of $H_2$ collected with time, wherein the slope of the plot dictates the rate of hydrogen production. The rate of hydrogen production is calculated to be 0.06 mL min$^{-1}$ cm$^{-2}$ (area-specific) and 60 mL min$^{-1}$ $g_{cat}^{-1}$ (catalyst mass-specific). While increasing the current density to 100 mA cm$^{-2}$, the $H_2$ production increased to 770 mL min$^{-1}$ g$^{-1}$, with a cell potential of −2.63 V (Fig. S19). Similarly, an AEM water electrolyser was assembled with an alkaline exchange membrane wherein the Ni-foam was used as an anode. It exhibits a cell potential of −1.80 V at 10 mA cm$^{-2}$, which exhibits a higher stability up to 100 hours (Fig. 6(b)). The rate of production of the $H_2$ gas is very similar to that in an acidic medium, as is shown in the inset of Fig. 6(b). The chronopotentiometry experiment was performed at a higher current density (100 mA cm$^{-2}$), exhibiting a cell potential of −2.70 V (Fig. S20).

Since WN/NC-1 exhibits excellent stability, post-mortem XPS analysis was conducted to determine the oxidation states of tungsten. The relative peak area was used to calculate the relative surface tungsten contents (Fig. S21). The ratio of $W^{3+}$ (WN) to $W^{6+}$ ($WO_3$) is largely unchanged (0.55) after the electrolysis in an acidic electrolyte. However, this value changes to 0.96 in an alkaline electrolyte, supporting the accelerated durability test results. The decrease in activity is attributed to the leaching of $WO_3$ (formed from WN) in the alkaline electrolyte, leading to the formation of $K_2WO_4$.

## Conclusions

Tungsten nitride (WN) on a carbon support was synthesised from the pyrolysis of urea, $Na_2WO_4 \cdot 2H_2O$ and porous carbon support (KB). The study of varying amounts of KB indicates that the carbon content enhances the conductivity and stabilises the WN nanoparticles. Thus, the synthesised WN/NC catalyst provides better performance towards the HER in both acidic (0.5 M $H_2SO_4$) and alkaline (1 M KOH) electrolytes. The overpotentials were estimated to be 200 and 230 mV for acidic and alkaline electrolytes, respectively. Additionally, the higher tungsten content material (WN/NC-1) exhibits better stability for up to 5000 cycles, demonstrating the robustness of the catalyst under extreme conditions. The mass-specific activity was estimated to be 24.2 A g$^{-1}$ in 0.5 M $H_2SO_4$ electrolyte, which is twice the amount of the $j_k$ value obtained in 1 M KOH electrolyte. The WN/NC-1 catalyst was tested as a cathodic electrocatalyst in water electrolysers. The PEM and AEM water electrolysers with the WN/NC-1 HER catalyst in the cathode provide $H_2$ at a rate of 770 mL min$^{-1}$ g$^{-1}$ at 100 mA cm$^{-2}$ in both acidic and alkaline electrolytes.
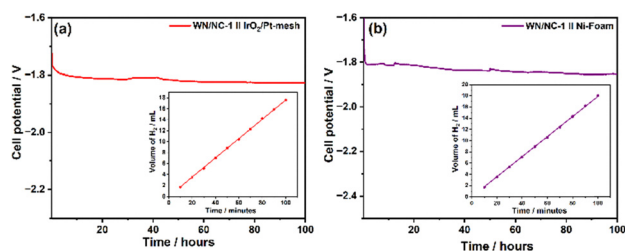


**Fig. 6** Chronopotentiometry curves of WN/NC-1-coated cathode water electrolysers: (a) 0.5 M $H_2SO_4$ (PEM) and (b) 1 M KOH (AEM) electrolytes at the constant current density of 10 mA cm$^{-2}$. The insets indicate the quantity of hydrogen evolved from the cathodes with time.

## Conflicts of interest

There are no conflicts to declare.

## Data availability

The data supporting this article have been included as part of the supplementary information (SI). The supplementary information contains control sample synthesis procedures; description of ECSA calculation; TOF calculation details; characterisation data for selected control samples; linear sweep voltammograms of control samples; photographs of electrolysers; XPS data after stability testing; additional supporting tables. See DOI: https://doi.org/10.1039/d5ya00253b.

## Acknowledgements

## References

1 I. Dincer and M. A. Rosen, *Appl. Energy*, 1999, **64**, 427–440.

2 P. F. Lang, *Sustainable Energy Fuels*, 2025, **9**, 4286–4293.

3 W. Lubitz and W. Tumas, *Chem. Rev.*, 2007, **107**, 3900–3903.

4 S. A. Ansari, M. W. Alam, N. Dhanda, M. S. Abbasi, M. E. Ahmed, A. B. alrashidi, A. M. Al-Farhan and B. Abebe, *Global Challenges*, 2025, **9**, 2500086.

5 Y. Li, L. Zhou and S. Guo, *EnergyChem*, 2021, **3**, 100053.

6 J. Zhang, C. Ma, S. Jia, Y. Gu, D. Sun, Y. Tang and H. Sun, *Adv. Energy Mater.*, 2023, **13**, 2302436.

7 X. Cheng, Y. Li, L. Zheng, Y. Yan, Y. Zhang, G. Chen, S. Sun and J. Zhang, *Energy Environ. Sci.*, 2017, **10**, 2450–2458.

8 A. Eftekhari, *Int. J. Hydrogen Energy*, 2017, **42**, 11053–11077.

9 J. Zhu, L. Hu, P. Zhao, L. Y. S. Lee and K. Y. Wong, *Chem. Rev.*, 2020, **120**, 851–918.

10 C. Das, N. Sinha and P. Roy, *Small*, 2022, **18**, 2202033.

11 F. Liu, C. Shi, X. Guo, Z. He, L. Pan, Z.-F. Huang, X. Zhang and J.-J. Zou, *Adv. Sci.*, 2022, **9**, 2200307.

12 Q. Fu, J. Han, X. Wang, P. Xu, T. Yao, J. Zhong, W. Zhong, S. Liu, T. Gao, Z. Zhang, L. Xu and B. Song, *Adv. Mater.*, 2021, **33**, 1907818.

13 S. Vijayapradeep, N. Logeshwaran, S. Ramakrishnan, A. Rhan Kim, P. Sampath, D. Hwan Kim and D. Jin Yoo, *Chem. Eng. J.*, 2023, **473**, 145348.

14 B. Zhou, J. Wang, L. Guo, H. Li, W. Xiao, G. Xu, D. Chen, C. Li, Y. Du, H. Ding, Y. Zhang, Z. Wu and L. Wang, *Adv. Energy Mater.*, 2024, **14**, 2402372.

15 Y. Zhong, X. Xia, F. Shi, J. Zhan, J. Tu and H. J. Fan, *Adv. Sci.*, 2016, **3**, 1500286.

16 H. Wang, J. Li, K. Li, Y. Lin, J. Chen, L. Gao, V. Nicolosi, X. Xiao and J.-M. Lee, *Chem. Soc. Rev.*, 2021, **50**, 1354–1390.

17 X. Peng, C. Pi, X. Zhang, S. Li, K. Huo and P. K. Chu, *Sustainable Energy Fuels*, 2019, **3**, 366–381.

18 Y. Abghoui and E. Skúlason, *J. Phys. Chem. C*, 2017, **121**, 24036–24045.

19 W.-F. Chen, J. T. Muckerman and E. Fujita, *Chem. Commun.*, 2013, **49**, 8896–8909.

20 L. Yu, S. Song, B. McElhenny, F. Ding, D. Luo, Y. Yu, S. Chen and Z. Ren, *J. Mater. Chem. A*, 2019, **7**, 19728–19732.

21 J. Xie and Y. Xie, *Chem. – Eur. J.*, 2016, **22**, 3588–3598.

22 Z.-G. Yang, H.-M. Xu, T.-Y. Shuai, Q.-N. Zhan, Z.-J. Zhang, K. Huang, C. Dai and G.-R. Li, *Nanoscale*, 2023, **15**, 11777–11800.

23 B. Liu, B. He, H.-Q. Peng, Y. Zhao, J. Cheng, J. Xia, J. Shen, T.-W. Ng, X. Meng, C.-S. Lee and W. Zhang, *Adv. Sci.*, 2018, **5**, 1800406.

24 H. Jin, X. Liu, A. Vasileff, Y. Jiao, Y. Zhao, Y. Zheng and S.-Z. Qiao, *ACS Nano*, 2018, **12**, 12761–12769.

25 N. S. Alhajri, H. Yoshida, D. H. Anjum, A. T. Garcia-Esparza, J. Kubota, K. Domen and K. Takanabe, *J. Mater. Chem. A*, 2013, **1**, 12606–12616.

26 M. Xiang, M. Song, Q. Zhu, Y. Yang, C. Hu, Z. Liu, H. Zhao and Y. Ge, *Chem. Eng. J.*, 2021, **404**, 126451.

27 X. Feng, H. Wang, X. Bo and L. Guo, *ACS Appl. Mater. Interfaces*, 2019, **11**, 8018–8024.

28 B. Zhang, C. Xiao, S. Xie, J. Liang, X. Chen and Y. Tang, *Chem. Mater.*, 2016, **28**, 6934–6941.

29 S. H. Park, T. H. Jo, M. H. Lee, K. Kawashima, C. B. Mullins, H.-K. Lim and D. H. Youn, *J. Mater. Chem. A*, 2021, **9**, 4945–4951.

30 S. Tang, B. Ouyang, H. Tan, W. Zhou, Z. Ma and Y. Zhang, *Electrochim. Acta*, 2020, **362**, 137222.

31 G. Sun, X. Liu, H. Mao, S. Wu, Y. Liu, T. Wang, J. Chi and L. Wang, *Inorg. Chem. Front.*, 2024, **11**, 682–712.

32 X. Kang, X.-H. Tan, N. Han, J.-F. Hou, C.-M. Yao, Z.-J. Chen and B.-J. Ni, *Tungsten*, 2024, **6**, 675–695.

33 B. Ren, D. Li, Q. Jin, H. Cui and C. Wang, *J. Mater. Chem. A*, 2017, **5**, 19072–19078.

34 P. Wei, X. Zhuge, Q. Li, X. Sun, W. Liu, K. Liang, J. Han, Y. Ren and Y. Huang, *J. Colloid Interface Sci.*, 2024, **662**, 814–821.

35 H. Jin, H. Zhang, J. Chen, S. Mao, Z. Jiang and Y. Wang, *J. Mater. Chem. A*, 2018, **6**, 10967–10975.

36 H. Yan, C. Tian, L. Wang, A. Wu, M. Meng, L. Zhao and H. Fu, *Angew. Chem., Int. Ed.*, 2015, **54**, 6325–6329.

37 S. Baskaran, E. A. A. Nazer and A. Muthukrishnan, *Sustainable Energy Fuels*, 2024, **8**, 1761–1768.

38 P. V. Geetha, A. N. Eledath and A. Muthukrishnan, *ACS Appl. Energy Mater.*, 2025, **8**, 10212–10225.

39 V. Chakrapani, J. Thangala and M. Sunkara, *Int. J. Hydrogen Energy*, 2009, **34**, 9050–9059.

40 O. Shebanova and P. McMillan, *High Press. Res.*, 2006, **26**, 87–97.

41 T. Li, L. Ye and K. Xie, *Int. J. Hydrogen Energy*, 2024, **58**, 822–828.

42 M. Thommes, K. Kaneko, A. V. Neimark, J. P. Olivier, F. Rodriguez-Reinoso, J. Rouquerol and K. S. W. Sing, *Pure Appl. Chem.*, 2015, **87**, 1051–1069.

43 C. Zhu, W. Zhou, M. Chen, K. Yuan, N. Chen, A. Wang, D. Zhao, L. Li, X. Liang and M. An, *Electrochim. Acta*, 2024, **489**, 144184.

44 C. C. L. McCrory, S. Jung, I. M. Ferrer, S. M. Chatman, J. C. Peters and T. F. Jaramillo, *J. Am. Chem. Soc.*, 2015, **137**, 4347–4357.

45 N. Logeshwaran, S. Vijayapradeep, A. R. Kim, P. Sampath, S. Ramakrishnan, M. B. Poudel, D. H. Kim and D. J. Yoo, *J. Energy Chem.*, 2023, **86**, 167–179.

46 N. Krstajić, M. Popović, B. Grgur, M. Vojnović and D. Šepa, *J. Electroanal. Chem.*, 2001, **512**, 16–26.

47 J. Wang, W. Zang, X. Liu, J. Sun, S. Xi, W. Liu, Z. Kou, L. Shen and J. Wang, *Small*, 2024, **20**, 2309427.

48 R. D. Armstrong and M. Henderson, *J. Electroanal. Chem. Interfacial Electrochem.*, 1972, **39**, 81–90.

49 G. M. Abd El-Hafez, N. H. Mahmoud, A. Walcarius and A. M. Fekry, *Int. J. Hydrogen Energy*, 2019, **44**, 16487–16496.

50 A. Loiacono, S. Díaz-Coello, G. García, G. I. Lacconi, J. Luis Rodriguez, E. Pastor and E. A. Franceschini, *J. Electroanal. Chem.*, 2024, **952**, 117973.

51 D. A. Harrington and B. E. Conway, *Electrochim. Acta*, 1987, **32**, 1703–1712.

52 P. Wei, X. Sun, M. Wang, J. Xu, Z. He, X. Li, F. Cheng, Y. Xu, Q. Li, J. Han, H. Yang and Y. Huang, *ACS Appl. Mater. Interfaces*, 2021, **13**, 53955–53964.

53 S. Baskaran, G. P. Mageswari and A. Muthukrishnan, *ChemCatChem*, 2025, **17**, e00598.

54 Y. Huang, X. Zhang, X. Ji, J. Yu, H. Zhang, X. Ma, X. Zhou, Z. Ding and T. Huang, *Fuel*, 2025, **381**, 133389.

55 S. Liang, P. Wang, M. Jing, H. Hu, S. Zhang, Z. Cang, Y. Zhao, H. Gong and J. Liu, *ACS Appl. Nano Mater.*, 2024, **7**, 11553–11559.

56 C. Xue, Y. Dong, K. Li, D. Li, T. Wang, H. Shao, D. Yin, X. Bo and X. Dong, *J. Alloys Compd.*, 2025, **1042**, 184102.

57 Z. Hong, Z. Xu, Z. Wu, H. Zhang, P. Li, X. Xu and S. Duo, *Appl. Surf. Sci.*, 2023, **608**, 155159.

58 C. Tyagi, C. Lagrost, V. Dorcet, F. Tessier and B. Fabre, *ACS Appl. Energy Mater.*, 2023, **6**, 6842–6850.